2009

Simulations and Measurements of Gas-Droplet Flows in Supersonic Jets Expanding into Vacuum

A Venkattraman
Purdue University

Alina A. Alexeenko
Purdue University - Main Campus, alexeenk@purdue.edu

41st AIAA Thermophysics Conference
22 - 25 June 2009, San Antonio, Texas

AIAA 2009-3751

Simulations and Measurements of Gas-Droplet Flows in Supersonic Jets Expanding into Vacuum

A. Venkattraman*, and A.A. Alexeenko†

School of Aeronautics & Astronautics, Purdue University, West Lafayette, IN 47907

Simulations and measurements of gas-droplet multiphase flows in application to supersonic expansions into vacuum have been considered and compared with each other. The experiments involved exposing a control surface to a supersonic plume from two different nozzles and measuring the size distribution of droplets at various locations. The simulations are based on the direct simulation Monte Carlo modeling of vapor-phase flow with a one-way coupling of droplet momentum and energy. The droplet trajectories are computed for the experimental conditions for droplets originating at the throat and lip of two different nozzles. The maximum droplet radius reaching the control surface and the variation of droplet size with angle predicted by the trajectory computations agree well with the measurements using Optical Microscopy.

I. Introduction

Supersonic flows expanding into vacuum are encountered in a number of applications including high-altitude plumes, spacecraft contamination and vacuum technology. Rebrov[1] summarizes the accumulated knowledge on structure of free jets from various types of nozzles including axially symmetric orifices, converging diverging nozzles and two-dimensional slits offering a reflection of modern trends and new possibilities in the study of free jets. A rough evaluation of such jet flows can be based on a simple analysis but more detailed presentations of field parameters require computational modeling taking into account various physics including multicomponent flows with chemical reactions and phase transitions. The rapid expansion of the gas into vacuum, through a converging-diverging nozzle might lead to its condensation resulting in the formation of droplets which could alter the plume properties significantly.

The study of gas-droplet flows in supersonic nozzles has been addressed in various applications[2–6] in the past. For example, plume induced contamination due to condensation on the nozzle walls during the thruster start-up and burn-out has been a critical issue for the International Space Station (ISS).[2,3] Empirical relations for the droplet number flux distribution as a function of droplet diameter and angle measured from the axis of the nozzle have been attempted in the past[7] for droplets attributed to incomplete combustion. However, the characterization, including size and mass fraction distribution, of droplets formed due to heterogeneous nucleation of the expanding gas on the nozzle walls has not been considered before. In this work, we present gas-droplet flow simulations and measurements of droplet size distribution on a surface exposed to plume flow obtained by the supersonic expansion of a metal vapor through a converging-diverging nozzle. Metal vapor expansions have fewer thermophysical model uncertainties and are often easier to experiment with, when compared to typical liquid propellants, and thus give an opportunity to study the wall condensation and droplet transport phenomena in more detail. The main goal of this paper is the prediction of size distribution of droplets formed due to condensation in a supersonic jet expanding into high vacuum.

The remainder of the paper is organized as follows: Section 2 deals with obtaining the solution to the gas flow field; Section 3 describes the droplet transport models used in this work; Section 4 presents, discusses and compares the results obtained from the simulations and the measurements with the last section reserved for conclusions.

*Graduate Student, Student Member
†Assistant Professor, AIAA Senior Member.

II. Flow Conditions

A schematic of the experimental set-up used for comparison with the computations is shown in Figure 1. The metal vapor expands through the converging-diverging nozzle into a region of very low pressure. The control surface on which the jet impinges is also shown. To account for flow rarefaction ranging from a

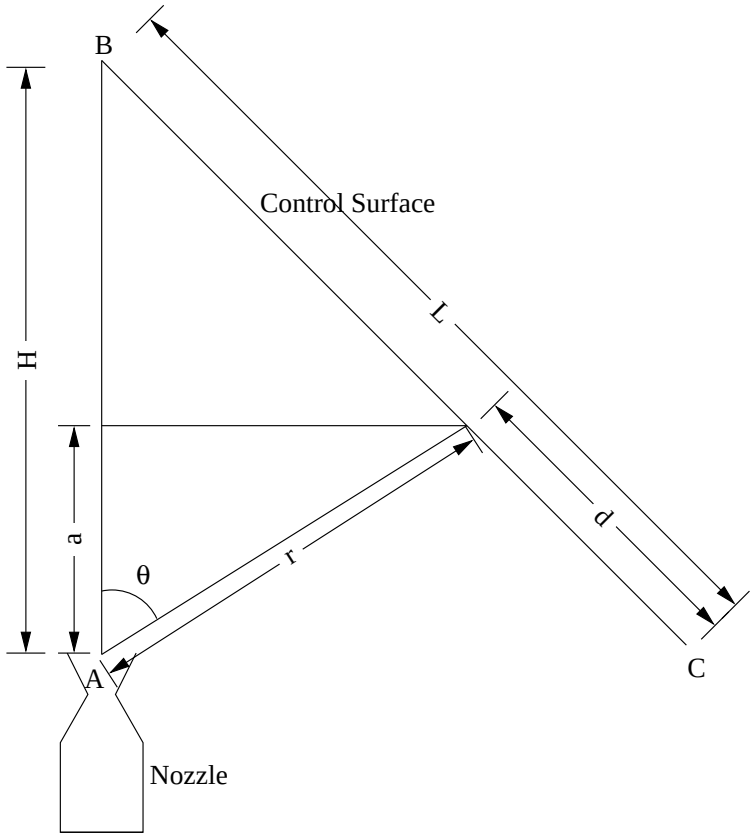

Figure 1. A schematic of the experimental set-up used for comparison with simulations.

near-continuum regime at the nozzle to the free-molecular flow in the far-field plume, the direct simulation Monte Carlo (DSMC) technique is applied to solve for the gas flowfields. The computations for the carrier gas phase, without accounting for droplets formed due to condensation, are performed using the 2D/Axi-symmetric version of the DSMC solver SMILE.[8] The molecular model is an important input to molecular approaches like the direct simulation Monte Carlo (DSMC) technique in order to ensure accurate modeling of the vapor phase. A Variable Hard Sphere (VHS) model with a reference diameter of $d_{ref} = 0.55\ nm$ and a viscosity-temperature exponent ($\omega = \alpha + 1/2$) of 0.81 is used in the DSMC simulations for intermolecular collisions of copper vapor. The values of the VHS parameters are chosen to capture the temperature dependence of viscosity coefficient predicted by the kinetic theory for Lennard-Jones interaction potential with parameters inferred from experimental data on cohesive energy at room temperatures.[9]

For the simulations in this work, the computational domain was divided into 115 collision cells in the x-direction and 80 collision cells in the y-direction. Each collision cell could further be divided into a maximum of 10 sub-cells in each direction. This ensured that the mean free path was greater than the size of the collision cell thereby ensuring that the process of selecting potential collision partners from the same collision cell is sufficiently accurate. The number of sampling cells was fixed at 520 in the x-direction and 400 in the y-direction with the possibility of further dividing each sampling cell into 10 sub-cells in each direction. The number of real to simulated molecules was chosen as $3{\times}10^{10}$ which was sufficient to provide good statistics for the cases considered in this work. All DSMC simulations were performed for a given value of the mass flow rate which mirrored the mass flow rates estimated from the experiments and was set by fixing the number density and temperature of the jet effusing from the nozzle.

Figures 2-4 compare contours of density, Mach number and Knudsen number for two cases with mass flow rates of 3.33e-6 kg/s and 7.5e-6 kg/s respectively. As the mass flow rate is increased, the flow becomes more collisional and hence the Kn decreases, as shown in Figure 3, moving towards the continuum regime. The contours of Mach number in Figure 4 indicate that the flow is supersonic at the exit of the source and in the low pressure chamber. The gas flow fields obtained using the DSMC simulations are then used as input to the droplet transport models in order to track the trajectory of droplets formed due to condensation of the expanding gas phase.

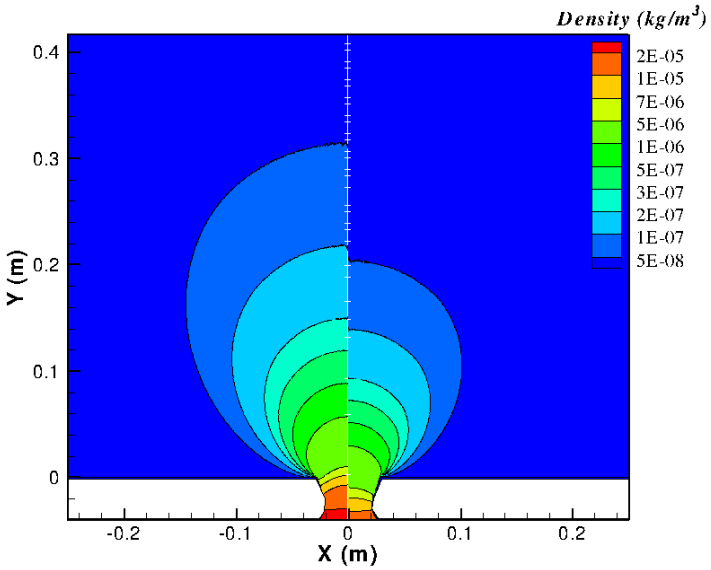

Figure 2. Comparison of density contours for $\dot{m}$ = 3.33e-6 kg/s (right) and $\dot{m}$ = 7.5e-6 kg/s (left)

III. Droplet Transport

The rapid expansion into vacuum leads to condensation of the metal vapor on the nozzle walls leading to the formation of droplets. The coupling between the two phases can be described either by a one-way coupling analysis, which assumes that the introduction of the droplet or the solid particle does not affect the flow field of the carrier gas phase, or by a two-way coupling analysis which accounts for the changes in the gas flow due to the introduction of the droplets or particles. All computations reported in this work use a one-way coupling analysis following the method described by Crowe *et.al.*[10] In multiphase flows, coupling between the gas phase and the droplet phase can occur through mass, momentum and energy coupling. Mass coupling in multiphase flows can occur through a number of mechanisms including evaporation of the droplet, condensation of the carrier gas or through chemical reactions. The key aspects of the momentum and energy coupling models used to compute the droplet trajectories presented in this work are discussed below.

III.A. Momentum Coupling

Momentum Coupling between the two phases can occur due to mass transfer and inter phase drag forces. This section discusses the momentum transfer due to drag forces on the droplet due to the relative velocity between the carrier gas and the droplet. Since the flow conditions in the current application correspond to the transition and rarefied regime, the expression for the drag coefficient should be valid over a wide range of Knudsen numbers. An empirical equation proposed by Crowe *et.al*[10] has been widely used in the past for modeling liquid and solid rocket propellant rocket nozzles and is given by

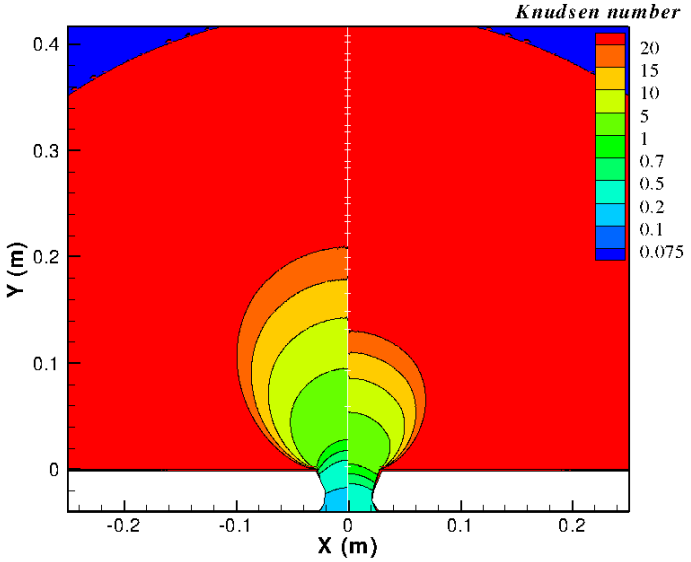

Figure 3. Comparison of contours of Kn for $\dot{m}$ = 3.33e-6 kg/s (right) and $\dot{m}$ = 7.5e-6 kg/s (left)

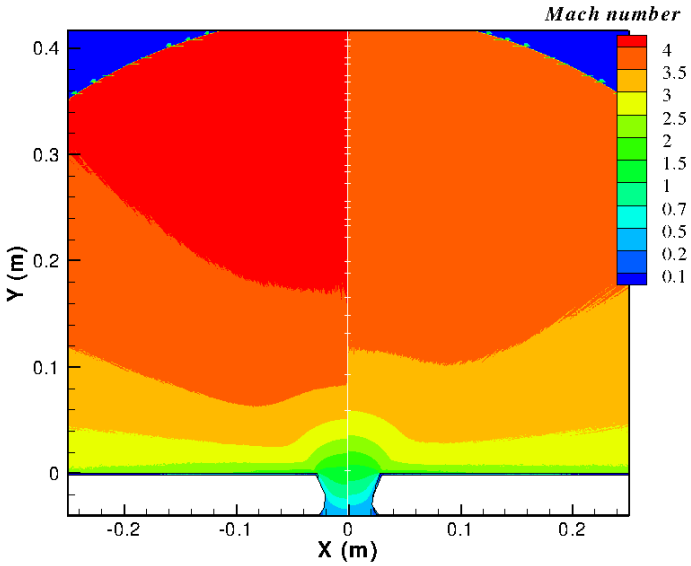

Figure 4. Comparison of contours of Mach number M for $\dot{m}$ = 3.33e-6 kg/s (right) and $\dot{m}$ = 7.5e-6 kg/s (left)

$$C_D = 2 + (C_{D_0} - 2)\exp\left(\frac{-3.07\sqrt{\gamma g(Re_r)M_r}}{Re_r}\right) + \frac{h(M_r)}{\sqrt{\gamma}M_r} exp\left(\frac{-Re_r}{2M_r}\right) \quad (1)$$

where M_r and Re_r refer to the Mach number and Reynolds number corresponding to the relative velocity between the droplet and gas phases.

$$Re_r = \frac{\rho_g V_{rel} D}{\mu_g} \quad (2)$$

$$M_r = \frac{V_{rel}}{\sqrt{\gamma R T_g}} \quad (3)$$

D is the diameter of the droplet. γ is the ratio of specific heats of the carrier gas (equals 5/3 for monatomic copper vapor). $g(Re)$ and $h(M)$ are correlations for Reynolds number and Mach number effects respectively.

$$g(Re) = \frac{1 + Re(12.278 + 0.548Re)}{1 + 11.278Re} \quad (4)$$

$$h(M) = \frac{5.6}{1+M} + 1.7\sqrt{\frac{T_d}{T_g}} \quad (5)$$

The final expression for the drag force on the droplet is given by

$$D = \frac{1}{2} C_D \rho_g V_{rel}^2 \frac{\pi d^2}{4} \quad (6)$$

III.B. Energy Coupling

Energy Coupling in multiphase flows can occur through radiation and convection. The radiative heat transfer is the net heat transfer to the droplet due to absorption and emission of radiant energy.

$$\dot{Q}_r = \pi D^2(\alpha J - e\sigma T_{\mathrm{d}}^4) \quad (7)$$

where α is the absorptivity of the particle material, J is the radiosity, σ is the Stefan-Boltzmann constant and e is the emissivity.

The convective heat transfer is given by

$$\dot{Q}_c = Nu\pi k_g D(T_g - T_d) \quad (8)$$

where Nu is the Nusselt number, k_g is the thermal conductivity of the carrier gas, T_g and T_d are the gas and droplet temperatures respectively. A correlation for the Nusselt number as a function of Reynolds number and Mach number that is valid for rarefied flows is given by

$$Nu = \frac{Nu_0}{1 + 3.42M_r/Re_r Pr} \quad (9)$$

where Nu_0 is the value at the incompressible flow limit and Pr is the Prandtl number = 2/3 for monatomic gases.

The differential equation governing the temperature of the droplet is then given by

$$mC_d \frac{dT_d}{dt} = \dot{Q}_r + \dot{Q}_c \quad (10)$$

where m is the droplet mass and C_d is the specific heat of the droplet. In the computations, no phase change has been considered and hence the energy equation does not account for the energy release during the phase change from liquid to solid. The heat transfer model was implemented in the droplet tracking code with following parameters.

$$e = 0.2$$

$$C_d = 385 \text{ J/kg/K}$$

IV. Results and Discussion

In this section, we present results obtained using simulations and make a comparison with measurements. The experiments involved a contact surface exposed to the plume flow and measuring the size of droplets deposited on the contact surface. As for the computations, the vapor phase flow obtained using DSMC simulations was used as in input to compute the trajectories of droplets introduced in the flow field.

IV.A. Computations

The models for droplet drag and heat transfer discussed above were incorporated by suitably modifying the Lagrangian particle tracking code developed for applications in liquid propellant engines[6] and then used to compute the trajectories for droplets of various sizes. The solution for the vapor phase flow obtained using DSMC simulations is used as an input to compute the droplet trajectories. The simulations were performed for two different nozzle geometries. In all further discussions, the nozzle with the larger throat diameter will be referred to as Nozzle 1 and the nozzle with the smaller throat diameter will be referred to as Nozzle 2. It should be mentioned that Nozzle 2 is not just a scaled down version of Nozzle 1. Droplets of various radii were introduced at a given location in the flow field and the variation of their position with time under the influence of the carrier gas was tracked.

The initial velocity of the droplets was chosen to be zero since the main source of droplets is likely to be condensation of the carrier gas on the walls of the nozzle which are then released from the walls into the flow field. The initial temperature of the droplets was fixed at 1300 K which is equal to the wall temperature at the nozzle throat. Apart from drag, the droplets are also under the influence of gravity. The gravitational force acts in the negative x-direction. Figures 5-8 compare the droplet trajectories for a mass flow rate of 1.11e-5 kg/s for droplets introduced at the throat and exit of the nozzles. It can be clearly seen that the maximum radius of droplets that reach the control surface is larger for Nozzle 2. Also, for each of the nozzles, the maximum radius of droplets is larger for droplets originating at the throat when compared to droplets originating at the lip of the nozzle. Specifically, for droplets originating at the throat, the maximum size of droplets that reach the control surface is 14 μm for Nozzle 1 whereas for Nozzle 2, it increases to 19 μm. Figures 9 and 10 show the contours of kinetic energy per unit volume for the two nozzles. The maximum kinetic energy per unit volume occurs in the vicinity of the throat and in the diverging section. It can be seen that Nozzle 2 has higher kinetic energy per unit volume. This indicates that the vapor flow in Nozzle 2 results in a larger momentum transfer to the liquid phase. This follows from the fact that for the same mass flow rate, Nozzle 2 has a higher mass flow rate per unit area and therefore higher kinetic energy per unit volume.

Next, the flow through Nozzle 1 at two different mass flow rates is considered. The mass flow rates chosen are 2.57e-6 kg/s and 5.75e-6 kg/s. Figures 11 and 12 show the trajectories for droplets of various radii corresponding to the two mass flow rates. The results indicate that, for the lower mass flow rate, the maximum size of droplets reaching the control surface is smaller when compared to the maximum size of droplets reaching the contact surface for the higher mass flow rate. While the maximum size of droplets reaching the contact surface is 6-7 μm for $\dot{m}$ = 5.75e-6 kg/s, it reduces to 2-3 μm for $\dot{m}$ = 2.75e-6 kg/s. The impact speeds of droplets of same radii become smaller for the lower mass flow rate case as shown in Table 1. The contours of kinetic energy per unit volume for two cases are shown in Figures 13 and 14 which, as expected, indicate that the kinetic energy per unit volume is higher for the higher mass flow rate simulation.

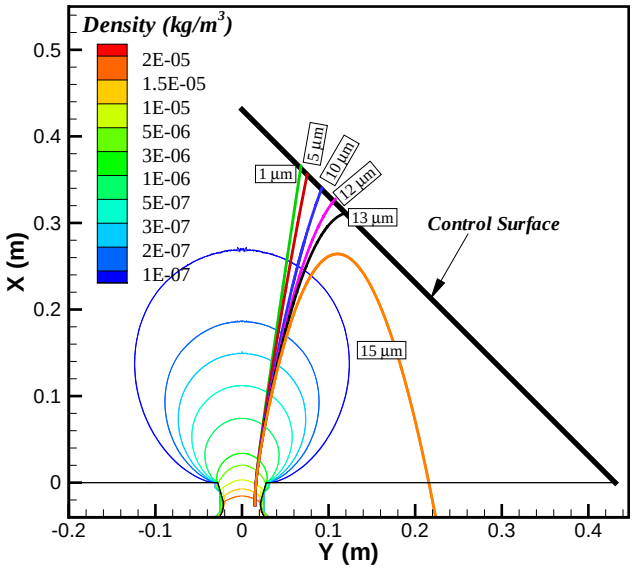

Figure 5. Comparison of trajectories of droplets of various radii originating at the nozzle throat for $\dot{m}$ = 1.11e-5 kg/s using Nozzle 1

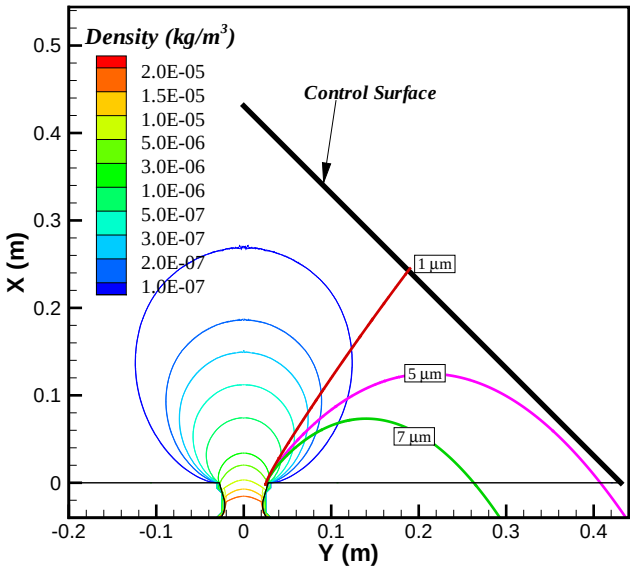

Figure 6. Comparison of trajectories of droplets of various radii originating at the nozzle lip for $\dot{m}$ = 1.11e-5 kg/s using Nozzle 1

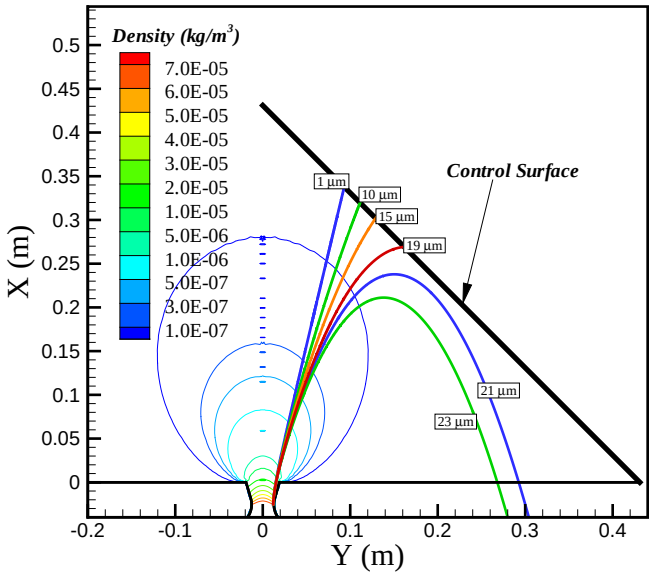

Figure 7. Comparison of trajectories of droplets of various radii originating at the nozzle throat for $\dot{m}$ = 1.11e-5 kg/s using Nozzle 2

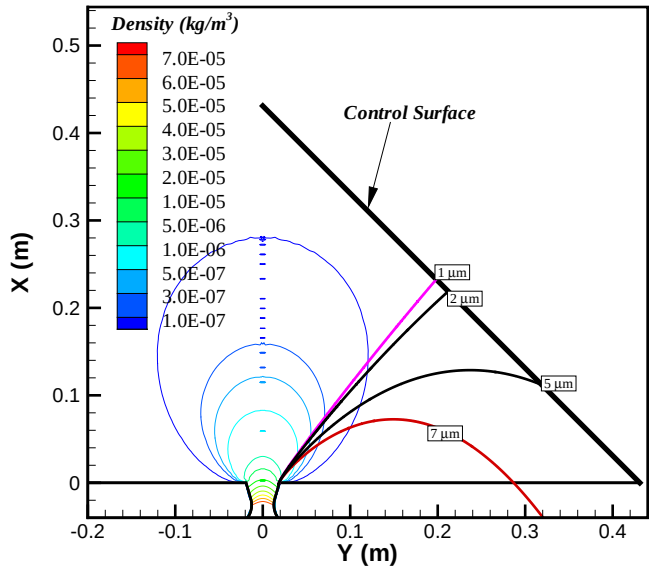

Figure 8. Comparison of trajectories of droplets of various radii originating at the nozzle lip for $\dot{m}$ = 1.11e-5 kg/s using Nozzle 2

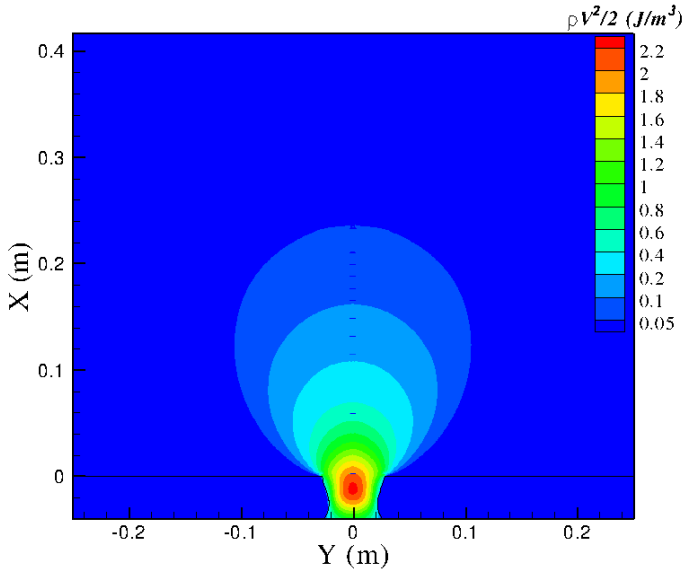

Figure 9. Contours of kinetic energy per unit volume in Nozzle 1 for $\dot{m}$ = 1.11e-5 kg/s

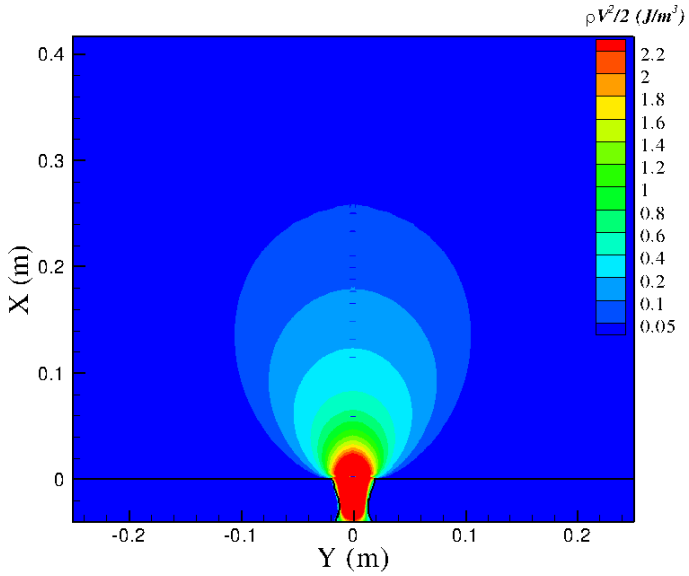

Figure 10. Contours of kinetic energy per unit volume in Nozzle 2 for $\dot{m}$ = 1.11e-5 kg/s

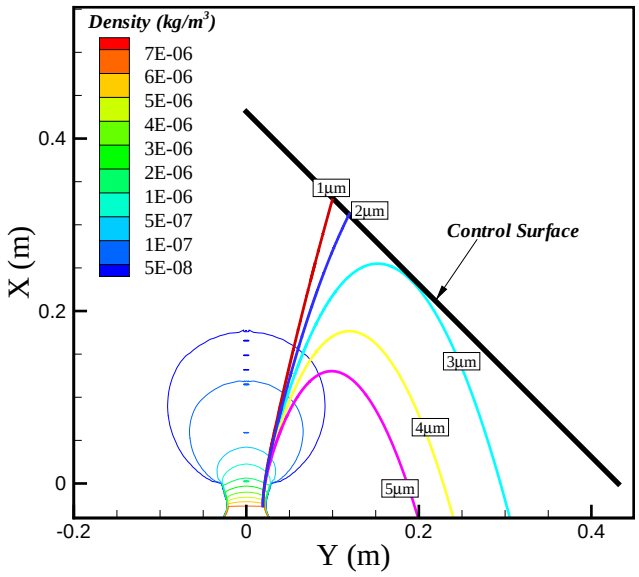

Figure 11. Droplet trajectories for Source 1 at a mass flow rate of 2.57e-6 kg/s

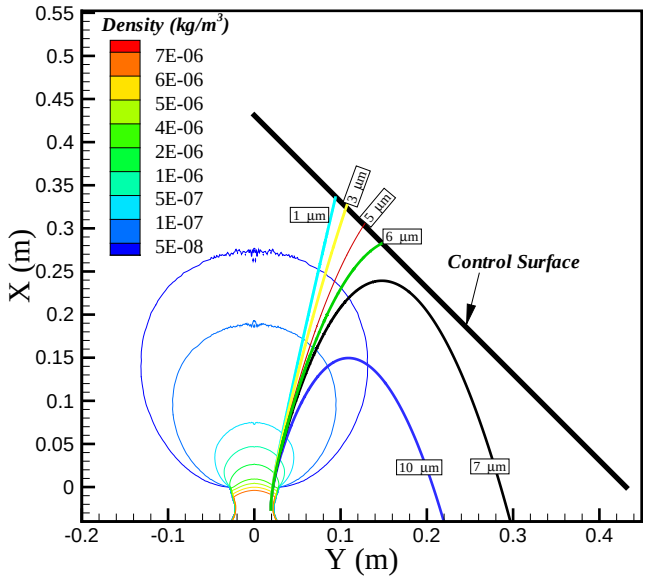

Figure 12. Droplet trajectories for Source 1 at a mass flow rate of 5.75e-6 kg/s

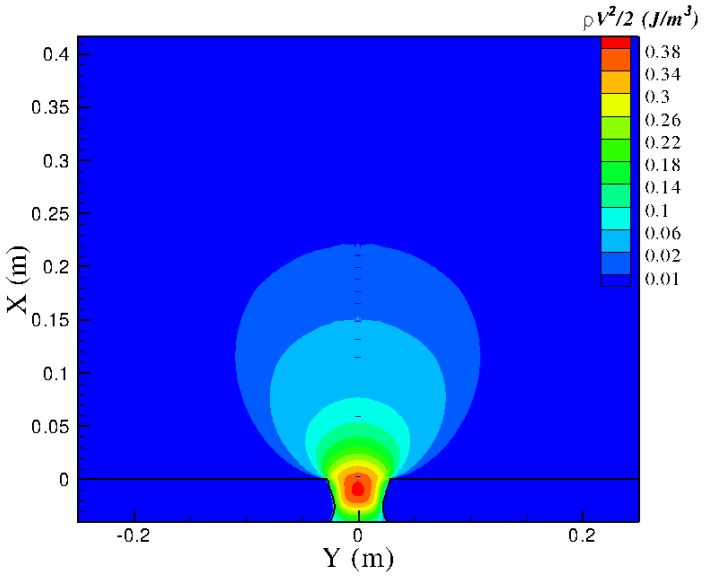

Figure 13. Droplet trajectories for Source 1 at a mass flow rate of 2.57e-6 kg/s

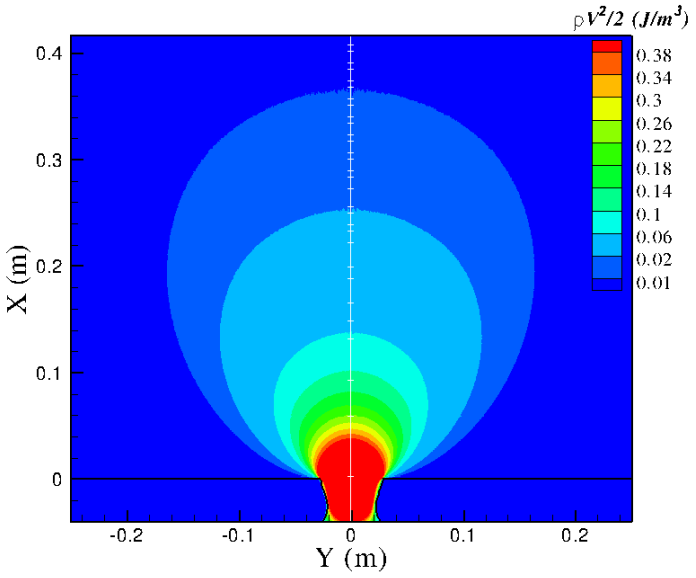

Figure 14. Droplet trajectories for Source 1 at a mass flow rate of 5.75e-6 kg/s

Table 1. Comparison of impact speeds of droplets of various radii for $\dot{m}$ = 2.57e-6 kg/s and $\dot{m}$ = 5.75e-6 kg/s

Radius (μm)	V_{impact} : $\dot{m}$ = 2.57e-6 kg/s (m/s)	V_{impact} : $\dot{m}$ = 5.75e-6 kg/s (m/s)
1	3	5.7
2	1.3	3.5
3	No Impact	2.4
4	No Impact	1.6
5	No Impact	1
6	No Impact	0.7

IV.B. Measurements

The measurements were performed using two different types of analysis techniques - Scanning Electron Microscopy and Optical Microscopy. This subsection presents and discusses the results obtained from the measurements.

IV.B.1. Scanning Electron Microscopy

Scanning Electron Microscopy(SEM) was performed at the School of Materials Engineering, Purdue University on the control surface exposed to Nozzle 1 at a mass flow rate of 1.11×10^{-5}. The images shown in Figure 15, indicates that the copper droplets are in the solid state when they reach the control surface. The droplets are spherical and there is no splashing or sloshing as would be the case if the droplets are in the liquid state when they reach the control surface. This is supported by Figure 16 which shows results obtained from computation for the temperature history of droplets of various sizes. The droplet temperature when it reaches the control surface is significantly lesser than the melting point of copper at the corresponding pressure. Additionally, in these SEM images, some of the droplets do not have a distinct edge and hence show that the droplets are produced at the nozzle and are deposited on the contact surface at different instants of time during the experiment.

IV.B.2. Optical Microscopy Analysis

Optical Microscopy was performed on a number of control surfaces exposed to two different nozzles and various mass flow rates. The images obtained by the optical microscopy technique, after conversion to a gray scale, were analyzed using an open source particle analysis software written in *java* - *ImageJ*. The software estimates the droplet area based on a threshold value set for the intensity. In further discussions, the location on the control surface that is closest to the axis of the nozzle is referred to as A, the location at approximately the middle of the control surface is referred to as B and the location of the control surface that is farthest from the axis is referred to as C. The corresponding angles measured from the axis of the nozzle are about 30°, 50° and 60° respectively.

The results obtained for all three control surfaces on which measurements were performed show a similar trend in which the maximum and mean radius of droplets increase from Location A to Location C which is exactly the same as the trend predicted by the droplet trajectory computations shown earlier. Also, the maximum radius of 14 μm predicted by droplet transport models for $\dot{m}$ = 7.5e-6 kg/s agrees well with the maximum radius of 16 μm obtained from optical microscopy measurements. The histograms, for the droplet radius obtained for $\dot{m} = 1.11e-5\ kg/s$, shown in 17 indicate that droplets of very small radius are not captured by the image analysis software and hence the droplet count does not go to zero for droplets of very small radii. Tables 2-4 shows the results for the maximum, mean droplet radii estimated from optical microscopy images for locations A, B, and C for various nozzle flow conditions.

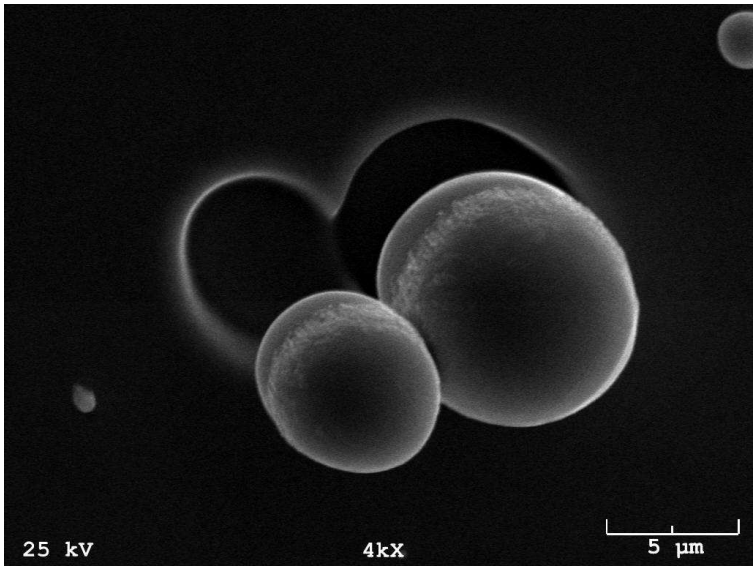

Figure 15. Scanning Electron Microscopy image of the contact surface exposed to Nozzle 1 at $\dot{m}$ = 1.11e-5 kg/s.

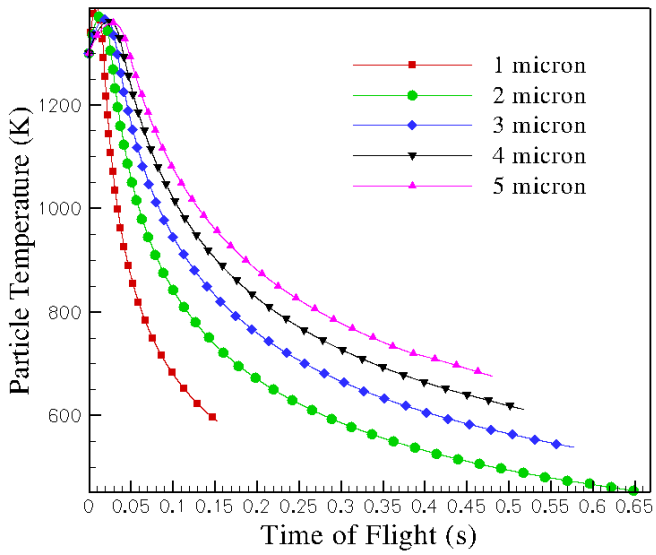

Figure 16. Temperature history of droplets of various sizes introduced at the nozzle throat

Table 2. Optical Microscopy results for the wafer obtained using Nozzle 1 and $\dot{m}$ = 1.11e-5 kg/s

Location	Max. Radius (μm)	Mean Radius (μm)	No. of Droplets	Area (mm^2)
A	8.0	1.8	623	0.27
B	9.6	2	746	0.27
C	16.7	3.7	819	1.35

Table 3. Optical Microscopy results for the wafer obtained using Nozzle 2 and $\dot{m}$ = 5.28e-6 kg/s

Location	Max. Radius (μm)	Mean Radius (μm)	No.of Droplets	Area (mm^2)
A	5.8	2.3	85	0.364
B	6.2	2.4	76	0.364
C	6.9	2.7	36	0.364

Table 4. Optical Microscopy results for the wafer obtained using Nozzle 2 and $\dot{m}$ = 2.78e-6 kg/s

Location	Max. Radius (μm)	Mean Radius (μm)	No.of Droplets	Area (mm^2)
A	2.3	1.4	16	0.3588
B	2.6	1.6	32	1.4352
C	3.7	1.8	41	1.4352

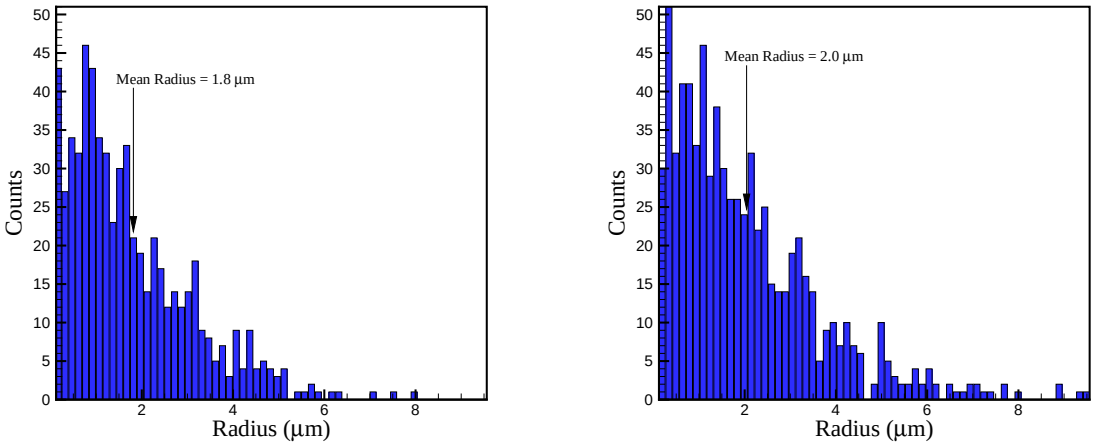

(a) Location A (b) Location B

Figure 17. Histogram of droplet radius for $\dot{m}$ = 1.11e-5 kg/s using Nozzle 1

V. Conclusions

Droplet transport models including momentum and energy coupling between the gas phase and the droplets were incorporated to compute the trajectories of droplets originating at the nozzle due to condensation of the rapidly expanding flow. The maximum size of droplets increased with increase in kinetic energy of the gas which in turn could be increased using a nozzle with a smaller throat area or a higher mass flow rate. The maximum size of droplets originating at the nozzle lip and reaching the control surface was smaller than for droplets originating at the throat. The droplets originating at the nozzle lip also reached the control surface at a location further away from the axis when compared to droplets originating at the throat. Optical Microscopy was performed on a number of control surfaces for various mass flow rates and two different nozzles. Comparisons with the computed droplet trajectories showed a good agreement for the maximum size of droplets reaching the control surface. As predicted by the droplet trajectory computations, the maximum size of droplets at a given control surface location increases with angle measured from the nozzle axis.

Acknowledgements

We would like to thank Dr. Tom Key of the School of Material Science and Engineering at Purdue for assistance with the SEM.

References

[1]A.K.Rebrov, "Free jets in vacuum technologies," *Journal of Vacuum Science and Technology A*, Vol. 19, No. 4, 2001, pp. 1679–1687.

[2]V.N.Yarygin, V.G.Prikhodko, I.V.Yarygin, Y., and A.N.Krylov, "Gas-Dynamic Aspects of the Contamination Problem at the International SpaceStation 1. Model Experiments," *Thermophysics and Aerodynamics*, Vol. 10(2), 2003, pp. 269–286.

[3]Yu.I.Gerasimov, A.N.Krylov, S.P.Sokolova, V.G.Prikhodko, V.N.Yarygin, I.V.Yarygin, S.G.Rebrov, and A.K.Buryak, "Gas-Dynamic Aspects of the Contamination Problem at the International Space Station 2. On Board Experiments," *Thermophysics and Aeromechanics*, Vol. 10(4), 2003, pp. 555–565.

[4]J.M.Burt and I.D.Boyd, "Evaluation of a Monte Carlo Model for Two Phase Rarefied Flows," *36th AIAA Thermophysics Conference*, AIAA, Orlando, Florida, 2003.

[5]M.S.Ivanov, D.V.Khotyanovsky, A.N.Kudryavtsev, P.V.Vashchenkov, G.N.Markelov, and A.A.Schmidt, "Numerical Study of Backflow for Nozzle Plumes Expanding into Vacuum," *37th AIAA Thermophysics Conference*, AIAA, Portland, Oregon, 2004.

[6]A.A.Alexeenko, D.C.Wadsworth, S.F.Gimelshein, and A.D.Ketsdever, "Numerical Modeling of ISS Thruster Plume Induced Contamination Environment," *SPIE 49th Annual Meeting*, SPIE, 2004.

[7]M.Larin, F.Lumpkin, and P.Stuart, "Modeling Unburned Propellant Droplet Distribution and Velocities in Plumes of Small Bipropellant Thrusters," *35th Thermophysics Conference*, AIAA, Anaheim, CA, 2001.

[8]M.S.Ivanov, A.V.Kashkovsky, S.F.Gimelshein, G.N.Markelov, A.A.Alexeenko, Ye.A.Bondar, G.A.Zhukova, S.B.Nikiforov, and P.V.Vaschenkov, "SMILE System for 2D/3D DSMC Computations," *25th International Symposium on Rarefied Gas Dynamics*, St.Petersburg, Russia, 2006.

[9]H.J.Hwang, O.K.Kwon, and J.W.Kang, "Copper nanocluster diffusion in carbon nanotube," *Solid State Communications*, Vol. 129, 2004, pp. 687–690.

[10]C.T.Crowe, M.Sommerfeld, and Y.Tsuji, *Multiphase Flows with Droplets and Particles*, CRC, New York, 1998.